Performance of Wrought Superalloys in Extreme Environments

B. A. Pint
Oak Ridge National Laboratory, P.O. Box 2008, Oak Ridge, TN 37831-6156 USA
(pintba@ornl.gov, 865-576-2897)

ABSTRACT

As power generation systems move towards higher efficiency operation above 700°C, wrought superalloys are the leading structural alloy candidates, including precipitation strengthened alloys 740 and 282 for the highest temperatures. To evaluate the performance of these alloys for these applications, a range of 500-5,000 h evaluations have been conducted in environments including steam, supercritical CO_2 (sCO_2) and simulated combustion exhaust with H_2O and/or SO_2 at 700°-800°C and compared to baseline exposures in laboratory air and 1 bar CO_2. These alloys primarily rely on the formation of an external Cr-rich oxide layer or scale for environmental protection and the reaction rates in all of these conditions are similar and relatively low. However, compared to a conventional solid solution strengthened alloy, like 625, the mass gains are higher due to the internal oxidation of the γ' forming additions, Al and Ti. Post-exposure characterization has quantified the reaction products and the depth of internal oxidation is not a concern and does not appear to increase above the baseline behavior in laboratory air. Likewise, there is no indication of internal carburization in the sCO_2 environment at 300 bar. The addition of 0.1% SO_2 in CO_2-10%H_2O at 800°C actually suppressed the internal oxidation at 1 bar but SO_2 may be a concern when the total pressure is higher.

Keywords: precipitation-strengthened wrought superalloys, extreme environments, supercritical CO_2, steam, environmental durability

INTRODUCTION

Nickel-based alloys are of increasing interest for power generation applications in order to enable higher temperature, and thus higher efficiency, operation. For fossil energy, the “least regret” strategy of generating less greenhouse gases in high efficiency systems [1] remains the most cost-effective method to reduce emissions (compared to carbon capture and sequestration). For concentrated solar power (CSP) applications, higher temperatures are needed to achieve the 50% efficiency goal for the steam or supercritical CO_2 (sCO_2) power block [2-4]. While Ni-base alloys are commonly used in combustion (i.e. natural gas-fired) turbines, the development of Ni-base alloys for the next generation of coal-fired power generation applications was led in the U.S. by the Advanced Ultra-supercritical consortium with a goal of increasing steam temperatures to 760°C/34.5 MPa (1400°F/5000 psi) [5-9]. Because of the high temperature and pressure goals, the consortium identified precipitate-strengthened alloys 740 (and 740H) and 282 [7,10-13] as the leading candidates and recognized their superior properties such that these alloys could lower materials costs for lower temperature applications by reducing the required wall thickness on pipes and tubes. The consortium successfully qualified alloy 740 in the ASME boiler and pressure vessel code and follow on work is in progress to qualify alloy 282. The allowable stresses for these alloys (estimates for 282) are shown in Figure 1. A significant strength advantage compared to previous alloys, particularly above 700°C, is obvious. The qualification of 740 is currently aiding the construction of a

50MW pilot plant for the sCO_2-based Allam power cycle [14], which has a goal to be the first clean fossil energy (initially using natural gas) power generation.

It has been well-established that Ni-base alloys with ~20+%Cr are very resistant to air and steam environments [12,15-20] and initial indications are that the same is true in sCO_2 environments [21-25]. Their resistance to fireside corrosion has been extensively studied up to 800°C [20,26-29]. Internal oxidation (IO) of the γ'-$Ni_3(Al,Ti)$ strengthening precipitates in 740 and 282 is a concern in all environments, especially in cast versions of these alloys [19]. However, exposure to steam did not affect the creep [12] or high cycle fatigue [30] behavior of this type of alloy. This study compiles various 500-5,000 h laboratory exposures of alloys 740 and 282 at 700°-800°C in environments including laboratory air, CO_2, sCO_2, steam and air with 10%H_2O (to simulate turbine exhaust) and compares their behavior to a conventional solid-solution alloy 625 [18,19,31,32]. While the Al and Ti additions result in higher parabolic rate constants in this temperature range, the rates are still reasonable low that there appears to be no environmental issue for deployment in these next generation power generation applications.

EXPERIMENTAL PROCEDURE

Compositions of the alloys used in this study are shown in Table 1. Oxidation coupons (typically 1.5 x 10 x 19mm) were machined and then hand polished to a 600 grit finish. Oxidation exposures were conducted for 100 or 500-h cycles. For oxidation in air, the coupons were placed in pre-annealed alumina boats or in individual alumina crucibles to catch any spalled oxide and the crucibles were placed in an alumina boat and slowly heated (2-4 h) and cooled in a resistively-heated box furnace or inserted and removed from a hot tube furnace with an alumina reaction tube. For 100h cycles in dry or "wet" (10vol.% H_2O) air or 500-h cycles in industrial grade (IG) 99.8% CO_2 (<120 ppm H_2O, <50 ppm O_2), the specimens were held in slotted boats to allow the gas to pass by the face of the specimen at 1-2cm/s. For the wet air test, endcaps were used on the alumina reaction tube and distilled deionized water was atomized into the carrier gas of filtered and dried air. Exposures in steam (atomized ~0.065µS/cm conductivity filtered, deaerated and deionized water with no carrier gas) were conducted in 500-h cycles at 17 bar in a high pressure test rig with an alloy 230 containment tube and the specimens held on a vertical alumina tube using Pt-10Rh wire [33]. The same system was used for exposures in research grade 99.995% CO_2 (<5 ppm H_2O, <5 ppm O_2), CO_2-10%H_2O and CO_2-10%H_2O-0.1%SO_2 with separate alloy 230 tubes at 1 and 25 bar [34]. The sCO_2 exposures were conducted in an alloy 282 autoclave operated at 300 bar of IG CO_2 with a ~1-2 ml/min flow rate and the specimens held on alumina rods with alumina spacers between specimens [22,23,25]. For the CO_2, sCO_2 and steam exposures, the specimens were slowly heated to temperature, held for 500 h and slowly cooled. Prior to exposure, all specimens were ultrasonically cleaned in acetone and ethanol and specimen mass changes were measured after exposures using a Mettler Toledo model XP205 balance (±0.04mg or ~0.01mg/cm^2 accuracy). For characterization, specimens were sectioned, Cu-plated and metallographically polished. Aqua regia etchant was used to highlight the internal oxidation zone for characterization. To quantify the scale thickness and internal oxidation, ImageJ software was used to analyze the light microscopy images. Typically, 30 measurements of oxide thickness and internal oxidation were made per specimen. Glow discharge optical emission spectroscopy (GDOES) was performed using a Horiba GD-Profiler 2 with a 4mm anode.

RESULTS AND DISCUSSION

700°C

Figure 2 shows specimen mass change data collected at 700°C in four environments. For the sCO_2 data, the values are the median values for 4-6 specimens (2 specimens removed after 1,000 h for characterization). The other data are single specimens. Small mass gains were observed in laboratory air, 17 bar steam and sCO_2. The decrease in mass observed in wet air for the 625 specimen is consistent with prior observation where the Cr_2O_3 scale reacts with H_2O to form a volatile $CrO_2(OH)_2$ reaction product:

$$1/2\ Cr_2O_3 + 3/4\ O_2(g) + H_2O(g) = CrO_2(OH)_2(g) \qquad (1)$$

resulting in a linear mass loss that depends on the temperature, gas flow velocity and water vapor content [35-39]. Figure 3 shows representative cross-sections from these exposures. Figure 3a-3c are etched to highlight the internal oxidation which results in adjacent γ′ depletion. The internal oxidation is relatively minor at this temperature. Figure 4 show the rate parabolic rate constants at this temperature, which were calculated using a standard process [40]. All of the rates measured at 700°C were significantly below the $5x10^{-13}$ $g^2cm^{-4}s^{-1}$ rate metric established for the 100,000 h CSP target lifetime (dashed line in Figure 4), which represents a mass gain of only ~ 13 mg/cm^2 and scale less than 100 μm after a 100,000 h exposure.

750°C

Longer exposures have been conducted at 750°C to develop a sCO_2 lifetime model with multiple specimens exposed in each condition [25]. Figure 5 shows the mass change data and the associated parabolic rate constants are shown in Figure 4. Median values for 6-10 specimens are shown for laboratory air, CO_2 and sCO_2 and individual specimen data are shown for steam. Most of the conditions at this temperature resulted in nearly parabolic behavior and the similar mass changes indicate little effect of CO2 pressure on the reaction rate. However, deviations from parabolic behavior are evident for all three alloys in laboratory air after ~3,000 h and more characterization is needed to clarify this behavior. Figure 6 shows representative cross-section for specimens exposed at 750°C. Figures 6a-6c show the reaction products after 5,000 h in 300 bar sCO_2 and Figures 6d-6f show similar images after 5,000 h in 1 bar IG CO_2. The minimal internal oxidation for the 625 specimens is evident compared to the 740 and 282 specimens. Little effect of CO_2 pressure was noted. Figures 6g-6i show 740 specimens after 1,000 h exposures in three different environments to include the shorter steam exposure.

To avoid relying on mass change for the lifetime model, specimens were periodically removed from the test for sectioning. Figure 7 shows box and whisker plots of the oxide thickness and depth of internal oxidation for 1 and 300 bar specimens exposed at 750°C. The boxes are defined by the 25%, median and 75% values and the whiskers show the minimum and maximum values measured. Similar measurements for specimens exposed in air are in progress as this test was recently completed as was the 5,000 h exposure in 1 bar CO_2. Consistent with the mass change data, the oxide thicknesses increase with exposure time and are very similar in the two conditions, Figure 7a. For the internal oxidation, the median values were slightly higher in 1 bar CO_2, although the differences are not significant. The measurements do not indicate the composition of the reaction product. Previous work in steam and laboratory air indicated mainly Al_2O_3 formed with a small amount of Ti-rich oxide [19]. To study C ingress, GDOES was used to profile the near-surface region. Figure 8 shows the Cr and C profiles for several 740 specimens exposed to 300 bar sCO_2 at 750°C. Depletion of Cr beneath the Cr-rich oxide is expected [23,36-39,41] as the Cr diffusion rate in the alloy is relatively slow. The C profiles show no indication of ingress. Instead, C depletion often coincides with the Cr depletion as has been explained based on an activity argument [43].

800°C

Figure 9 shows mass change data for four conditions at 800°C, where 5,000 h data were available in air and 17 bar steam [19,31]. Similar to the observation in wet air at 700°C, mass losses were observed for the 282 and 625 specimens with increasing mass loss observed for the 282 specimen after 4,000 h. The air and steam mass gains were similar for the 625 specimens but not for the other alloys. The 740 specimen exposed in air did not show parabolic behavior like the 625 and 282 specimens. Only 1,000 h exposures were conducted in 300 bar sCO_2 at 800°C as this is near the maximum operating conditions for the autoclave.

The sCO_2 mass gains are the median values for 6 specimens whereas the other values are single specimens. For the specimens showing parabolic behavior, the measured rate constants are plotted in Figure 4. One of the distinctive observations in Figure 4 is that whereas 740 showed lower rates at 700° and 750°C compared to 282, at 800°C the rates were more similar resulting in a higher activation energy for 740 compared to 625 and 282.

Figure 10 shows representative microstructures observed at 800°C. Figures 10a-10c show specimens after 1,000 h in sCO_2 and Figure 10d-10f show specimens after 5,000 h in 17 bar steam. Consistent with the mass gain data at 800°C, the oxide thickness and internal oxidation were similar for 740 and 282. Figure 10g and 10h show 625 and 282 specimens exposed to wet air, respectively. Figures 10h and 10i compare the 282 specimens exposed without and with H_2O. The thinner surface oxide after exposure in wet air may be due the $CrO_2(OH)_2$ evaporation. While one may draw conclusions about the relative behavior from these images about, for example, environmental effects on internal oxidation, a detailed quantitative study comparing air, wet air and 17 bar steam was reported previously [31]. As an example, Figure 11 shows the data reported at 800°C for alloy 282 specimens indicating very little difference among the three environments. The 1,000 h data for sCO_2 was added for comparison and shows a similar amount of internal oxidation.

Previously, work comparing the performance of Ni-based alloys in steam at 800°C [19] used the alloy Al+Ti content to show an increasing trend in mass gain after 5,000 h exposures at 800°C in 17 bar steam, Figure 12. While similar 5,000 h exposures have not been conducted in sCO_2, the shorter exposures at 800°C and similar exposures at 750°C were added for comparison including data being collected for alloys 230 and 617. In all cases, the there is an upward trend with Al and Ti content. While the obvious difference among these alloys in Figure 10 is the amount of internal oxidation, the thickness of the surface oxide is primarily related to the increased mass gain [19].

For the open or direct-fired Allam cycle [14], impurities from the combustion of natural gas or coal-derived synthesis gas are a significant concern for long-term compatibility. However, experimental equipment allowing impurity studies in sCO_2 conditions has only recently become available [24]. While waiting for the development of new laboratory equipment to address H_2O and O_2 impurities in sCO_2, initial work was conducted at 1 and 25 bar using 500 h exposures at 700° and 800°C [34]. Figure 13 shows cross-sections illustrated some of the initial findings for alloy 282 specimens. Relatively minor changes in mass (average of 3 specimens per condition) were observed among the six conditions. The addition of H_2O and change in pressure appeared to have little effect, perhaps with a reduction in internal oxidation with increasing pressure as suggested in Figure 7b. However, the addition of 0.1%SO_2 at 1 bar significantly reduced the oxide thickness and internal oxidation whereas increasing the pressure resulted in increased oxide thickness and internal oxidation. A similar beneficial effect of SO_2 has been observed for Fe-based alloys with the hypothesis that S is poisoning surface reaction or transport through the oxide [42]. However, that study only examined SO_2 effects at 1 atm. Further studies of impurity effects are in progress with a particular interest in the effect of pressure.

Finally, the long-term goal is to develop a predictive model for these various environments. The current effort is focused on sCO_2 conditions at 750°C. Figure 14a shows a simple extrapolation of the rate constants measured at 750°C. Interestingly, while a rate constant can be determined from only 2 data points after 1,000 h (mass gain after 500 and 1,000 h). The rate constant measured after a 6,000 h exposure was not significantly different. Figure 14b makes a similar extrapolation using the oxide thickness data in Figure 7a. The mass gain in Figure 14a can be converted to an oxide thickness assuming a dense Cr_2O_3 reaction product. In comparison, the oxide thickness values in (a) and (b) are similar and represent very thin oxides after extended service in this environment.

SUMMARY

A comparison of the reaction rates in several different oxidizing environments at 700°-800°C for solid solution (alloy 25) and precipitation strengthened (alloys 740 and 282) Ni-based alloys showed very little effect of environment on behavior compared to oxidation in laboratory air. The most significant exception was the wet air (simulated exhaust gas environment with 10%H_2O) where mass losses were observed due to the evaporation of a volatile Cr oxy-hydroxide. In all cases, the Al and Ti additions were observed to internally oxidize following a parabolic relationship with exposure time with little effect of environment on the rates of mass gain or depth of internal attack. The lack of significant corrosion problems suggests a potential opportunity for Ni-based alloys to enable much higher efficiencies for future fossil energy power generation cycles as well as concentrated solar power. The remaining issue currently being investigated is the effect of ~1% O_2 and ~0.3% H_2O in directed-fired sCO_2 cycles on 750°C reaction rates at 300 bar.

ACKNOWLEDGMENTS

The 700-750°C steam oxidation extracted from ORNL projects led by I. G. Wright. The current experimental work was conducted by M. Lance (GDOES), M. Howell, T. Lowe and T. Jordan. S. S. Raiman and J. Jun provided useful comments on the manuscript. This research was funded by the U.S. Department of Energy, Office of Energy Efficiency and Renewable Energy, Solar Energy Technology Program (SunShot Initiative) and by the Office of Fossil Energy, Crosscutting Research Program.

REFERENCES

1. Summerfield IR, Goldthorpe SH and C. J. Bower (1993) Combating Global Warming–Reducing CO_2 Emissions from Coal-Fired Power Plant. Proc. Inst. Mech. Eng. A–J. Power Energy 207(A2):81-88.
2. Feher EG (1968) The Supercritical Thermodynamic Power Cycle. Energy Conversion 8:85-90.
3. B. D. Iverson, T. M. Conboy, J. J. Pasch and A. M. Kruizenga, “Supercritical CO_2 Brayton cycles for solar-thermal energy,” Applied Energy, 111 (2013) 957-970.
4. V. T. Cheang, R. A. Hedderwick, C. McGregor, “Benchmarking supercritical carbon dioxide cycles against steam Rankine cycles for Concentrated Solar Power,” Solar Energy, 113 (2015) 199-211.
5. Viswanathan R, Bakker W (2001) Materials for Ultrasupercritical Coal Power Plants–Boiler Materials: Part I. J. Mater. Eng. Perform. 10(1):81-95.
6. Viswanathan R, Bakker W (2001) Materials for Ultrasupercritical Coal Power Plants–Turbine Materials: Part II. J. Mater. Eng. Perf. 10(1):96-101.
7. R. Viswanathan, J.F. Henry, J. Tanzosh, G. Stanko, J. Shingledecker, B. Vitalis, and R. Purgert, “U.S. Program on Materials Technology for Ultra-Supercritical Coal Power Plants,” J. Mater. Eng. Performance 14, 3 (2005): pp.281-285.
8. R. Viswanathan, J. Sarver and J. Tanzosh, “Boiler Materials for Ultra-Supercritical Coal Power Plants – Steamside Oxidation,” J. Mater. Eng. Perf. 15, 3 (2006): pp.255-274.
9. R. Viswanathan, J. Shingledecker, and R. Purgert, “Evaluating Materials Technology for Advanced Ultrasupercritical Coal-Fired Plants,” Power 154, 8 (2010): pp.41-45.
10. S. Q. Zhao, X. S. Xie, G. D. Smith and S. J. Patel, “Microstructural stability and mechanical properties of a new nickel based superalloy,” Mater. Sci. Eng. A 355 (2003) 96-105.
11. L. M. Pike, “Development of a Fabricable Gamma-Prime (γ') Strengthened Superalloy,” in Superalloys 2008, R. C. Reed et al. eds TMS, Warrendale, PA, 2008, pp.191-200.

12. S. Dryepondt, K. A. Unocic and B. A. Pint, “Effect of Steam Exposure on the Creep Properties of Ni-based Alloys,” Mater. Corros. 63 (2012): pp.889-895.
13. J. J. deBarbadillo, B. A. Baker and R. D. Gollihue, “Nickel-Base Superalloys for Advanced Power Systems – An Alloy Producer’s Perspective,” in Proceedings of the 4th International Symposium on Supercritical CO_2 Power Cycles, Pittsburgh, PA, September 2014, Paper #3.
14. Allam RJ, M. R. Palmer, G. W. Brown Jr., J. Fetvedt, D. Freed, H. Nomoto, M. Itoh, N. Okita, C. Jones Jr C (2013) High efficiency and low cost of electricity generation from fossil fuels while eliminating atmospheric emissions, including carbon dioxide. Energy Procedia 37:1135–1149.
15. W. E. Ruther and S. Greenberg, “Corrosion of Steels and Nickel Alloys in Superheated Steam,” J. Electrochem. Soc. 111 (1964): pp.1116-1121.
16. G. C. Wood, I. G. Wright, T. Hodgkiess, D. P. Whittle, "A Comparison of the Oxidation of Fe-Cr, Ni-Cr and Co-Cr Alloys in Oxygen and Water Vapor," Werk. Korr. 21 (1970): pp.900-910.
17. K. Natesan and J.H. Park, “Fireside and steamside corrosion of alloys for USC plants,” Inter. J. Hydrogen Energy 32 (2007): pp.3689-3697.
18. I. G. Wright and R. B. Dooley, “A review of the oxidation behavior of structural alloys in steam,” Inter. Mater. Rev. 55, 3 (2010): pp.129-167.
19. E. Essuman, L. R. Walker, P. J. Maziasz and B. A. Pint, “Oxidation Behavior of Cast Ni-Cr Alloys in Steam at 800°C,” Mater. Sci. Technol. 29 (2013): pp.822-827.
20. G. Stein-Brzozowska, D. M. Flórez, J. Maier, G. Scheffknecht, “Nickel-base superalloys for ultra-supercritical coal-fired power plants: Fireside corrosion. Laboratory studies and power plant exposures,” Fuel 108 (2013): pp.521–533.
21. R. I. Olivares, D. J. Young, P. Marvig and W. Stein, “Alloys SS316 and Hastelloy-C276 in Supercritical CO_2 at High Temperature,” Oxid. Met. 84 (2015) 585–606.
22. B. A. Pint and J. R. Keiser, “Initial Assessment of Ni-Base Alloy Performance in 0.1 MPa and Supercritical CO_2,” JOM 67(11) (2015) 2615-2620.
23. B. A. Pint, R. G. Brese and J. R. Keiser, “Effect of Pressure on Supercritical CO_2 Compatibility of Structural Alloys at 750°C,” Materials and Corrosion, 68 (2017) 151-158.
24. J. Mahaffey, D. Adam, A. Brittan, M. Anderson and K. Sridharan, “Corrosion of Alloy Haynes 230 in High Temperature Supercritical Carbon Dioxide with Oxygen Impurity Additions,” Oxidation of Metals 86 (2016) 567-580.
25. Pint BA, K. A. Unocic, R. G. Brese and J. R. Keiser JR (2017) Characterization of Chromia Scales Formed in Supercritical Carbon Dioxide,” Materials at High Temperature, in press.
26. N. Mu, K. Y. Jung, N. M. Yanar, G. H. Meier, F. S. Pettit, G. R. Holcomb, Water Vapor Effects on the Oxidation Behavior of Fe-Cr and Ni-Cr Alloys in Atmospheres Relevant to Oxy-fuel Combustion, Oxid. Met. 78 (2012): pp.221-237.
27. G. R. Holcomb, J. Tylczak, G. H. Meier, K. Y. Jung, N. Mu, N. Yanar, F. Pettit, “Fireside Corrosion in Oxy-Fuel Combustion of Coal,” ECS Transactions, 41, 42 (2012): pp.73-84.
28. B. A. Pint and J. K. Thomson, “Effect of Oxy-Firing on Corrosion Rates at 600°-800°C,” NACE Paper 13-2171, Houston, TX, presented at NACE Corrosion 2013, Orlando, FL, March 2013.
29. B. A. Pint, (2014) “The Use of Model Alloys to Study the Effect of Alloy Composition on Steam and Fireside Corrosion,” NACE Paper 14-4279, Houston, TX, presented at NACE Corrosion 2014, San Antonio, TX, March 2014.
30. A. Shyam, C. S. Hawkins, R. Shibayan, S. Dryepondt, D. L. Erdman III and P. J. Maziasz, “The Effect of Steam on the Elevated Temperature High Cycle Fatigue Life of Haynes 282® Superalloy,” in Proc. 10th Liege Conference on Materials for Advanced Power Engineering, Liege, Belgium, Sept. 2014.
31. Pint BA, Thiesing BP (2015) “Effect of Environment on the Oxidation Behavior of Commercial and Model Ni-Base Alloys,” NACE Paper C2015-5919, Houston, TX, presented at NACE Corrosion 2015, Dallas, TX, March 2015.

32. S. Dryepondt, S. J. Jones, Y. Zhang, P. J. Maziasz and B. A. Pint, “Oxidation, Creep and Fatigue Properties of Bare and Coated 31V Alloy,” JOM 67 (2015) 68-76.
33. K. A. Terrani, B. A. Pint, C. M. Parish, C. M. Silva, L. L. Snead and Y. Katoh, “Silicon Carbide Oxidation in Steam up to 2 MPa,” J. Am. Ceram. Soc. 97 (2014) 2331-2352.
34. B. A. Pint, R. G. Brese and J. R. Keiser, “The Effect of Impurities and Pressure on Oxidation in CO_2 at 700°-800°C,” NACE Paper C2018-11199, Houston, TX, presented at NACE Corrosion 2018, Phoenix, AZ, April 2018.
35. H. Asteman, J.-E. Svensson, L.-G. Johansson and M. Norell “Indication of Chromium Oxide Hydroxide Evaporation During Oxidation of 304L at 873K in the Presence of 10% Water Vapor,” Oxid. Met. 52 (1999): pp.95-111.
36. B. A. Pint, “The Effect of Water Vapor on Cr Depletion in Advanced Recuperator Alloys,” ASME Paper #GT2005-68495, presented at the International Gas Turbine & Aeroengine Congress & Exhibition, Reno-Tahoe, NV, June 6-9, 2005.
37. D. J. Young and B. A. Pint, “Chromium Volatilization Rates from Cr2O3 Scales into Flowing Gases Containing Water Vapor,” Oxid. Met. 66 (2006): pp.137-153.
38. J. M. Rakowski, C. P. Stinner, M. Lipschutz and J. P. Montague, “Metallic Alloys for Primary Surface Recuperators,” ASME Paper #GT2006-90680, presented at the International Gas Turbine & Aeroengine Congress & Exhibition, Barcelona, Spain, May 8-11, 2006.
39. Pint BA (2006) Stainless Steels with Improved Oxidation Resistance for Recuperators. J. Eng. Gas Turb. & Power 128:370-376.
40. Pieraggi B (1987) Calculations of Parabolic Reaction Rate Constants. Oxidation of Metals 27:177-185.
41. Evans HE, Lobb RC (1984) Alloy Depletion Profiles During Non-Protective Oxidation. Corrosion Science 24:223-236.
42. Yu C, Zhang J, D. J. Young DJ (2016) High temperature corrosion of Fe-Cr-(Mn/Si) alloys in CO_2-H_2O-SO_2 gases. Corrosion Science 112:214–225.

Figure Captions

Figure 1. ASME boiler and pressure vessel code allowable stresses as a function of operating temperature for several Fe- and Ni-base alloys.

Figure 2. Specimen mass change data at 700°C for alloy specimens in four environments.

Figure 3. Light microscopy of specimens exposed at 700°C (a) 625, 1,000 h in sCO_2, (b) 740, 1,000 h in sCO_2, (c) 282, 1,000 h in sCO_2, (d) 625, 2,000 h in sCO_2, (e) 740, 1,000 h in 17 bar steam and (f) 740, 4,000 h in 17 bar steam. (a-c) are etched in aqua regia.

Figure 4. Arrhenius plot of parabolic rate constants measured in this study in four environments.

Figure 5. Specimen mass change data at 750°C for alloy specimens in four environments.

Figure 6. Light microscopy of specimens exposed at 750°C (a) 625, 5,000 h in sCO_2, (b) 740, 5,000 h in sCO_2, (c) 282, 5,000 h in sCO_2, (d) 625, 5,000 h in CO_2, (e) 740, 5,000 h in CO_2, (f) 282, 5,000 h in CO_2, (g) 740, 1,000 h in lab. Air, (h) 740, 1,000 h in 17 bar steam and (i) 740, 1,000 h in CO_2.

Figure 7. Box and whisker plots of the (a) oxide thickness and (b) depth of internal oxidation after exposures in 1 and 300 bar CO_2 at 750°C. The median value is shown.

Figure 8. Glow discharge optical emission profiles for alloy 740 specimens exposed at 750°C to 300 bar sCO_2 for various times compared to an as-received specimen. There was no evidence of C ingress into the substrate after exposure but Cr depletion beneath the scale was evident.

Figure 9. Specimen mass change data at 800°C for alloy specimens in four environments.

Figure 10. Light microscopy of specimens exposed at 800°C (a) 625, 1,000 h in sCO_2, (b) 740, 1,000 h in sCO_2, (c) 282, 1,000 h in sCO_2, (d) 625, 5,000 h in 17 bar steam, (e) 740, 5,000 h in 17 bar steam, (f) 282, 5,000 h in 17 bar steam, (g) 625, 6,000 h in wet air, (h) 282, 5,000 h in wet air and (i) 282, 5,000 h in lab. air.

Figure 11. Box and whisker plots of the depth of internal oxidation on alloy 282 specimens after exposures in four environments. The median value is shown.

Figure 12. Specimen mass gain after several different exposures plotted versus the Al+Ti content of the alloys. All conditions show the same increasing trend.

Figure 13. Light microscopy of alloy 282 specimens exposed for 500 h at 800°C at (a-c) 1 bar and (d-f) 25 bar in (a,d) high purity CO_2, (b,e) CO_2+10%H_2O and (c,f) CO_2+10%H_2O+0.1%SO_2.

Figure 14. (a) Extrapolation of the rate constants determined at 750°C after 1,000 and 6,000 h exposures in 300 bar sCO_2. The mass gain can be converted to an oxide thickness assuming a dense Cr_2O_3 reaction product. (b) Extrapolation of the oxide thickness data observed at 1,000-5,000 h in 300 bar sCO_2 to 100,000 h assuming parabolic behavior. The oxide thickness values in (a) and (b) are similar and represent very thin oxides after extended service in this environment.

Table 1. Chemical composition of the alloys measured by inductively coupled plasma and combustion analyses in mass%.

Alloy	**Ni**	**Cr**	**Fe**	**Co**	**Mo**	**Nb**	**Al**	**Ti**	**Si**	**Mn**	**C**
625	60.6	21.7	4.0	0.1	9.4	3.6	0.09	0.2	0.2	0.1	0.016
282	58.0	19.3	0.2	10.3	8.3	<	1.5	2.2	0.06	0.1	0.059
740	48.2	23.4	1.9	20.2	0.3	2.1	0.8	2.0	0.5	0.3	0.027

< denotes less than 0.002

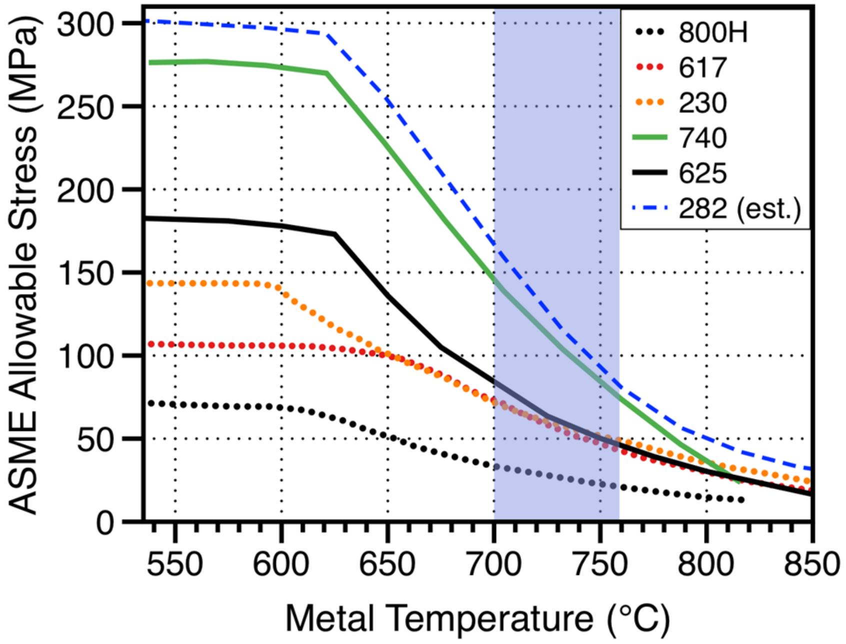

Figure 1. ASME boiler and pressure vessel code allowable stresses as a function of operating temperature for several Fe- and Ni-base alloys.

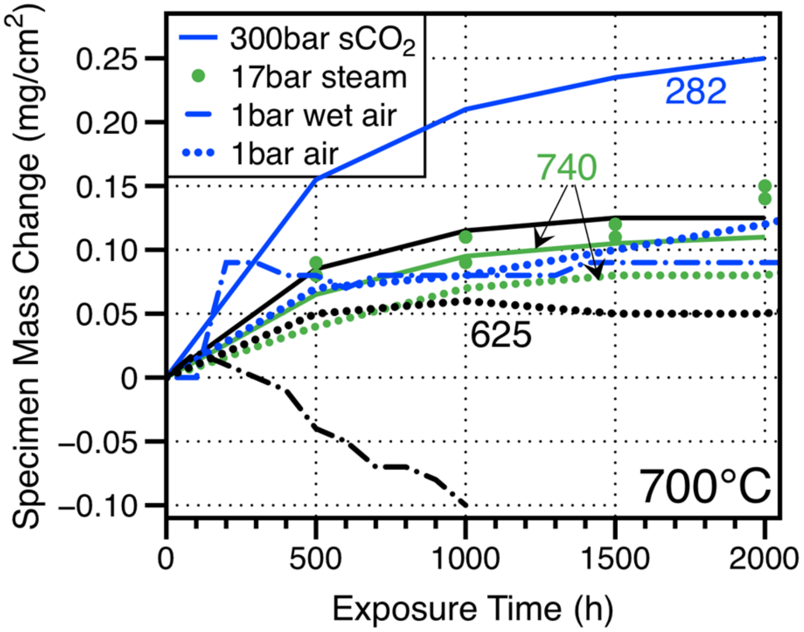

Figure 2. Specimen mass change data at 700°C for alloy specimens in four environments.

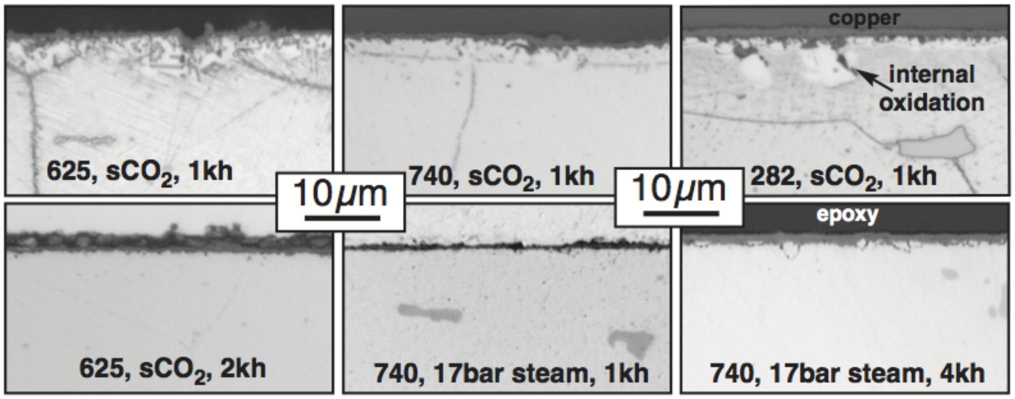

Figure 3. Light microscopy of specimens exposed at 700°C (a) 625, 1,000 h in sCO$_2$, (b) 740, 1,000 h in sCO$_2$, (c) 282, 1,000 h in sCO$_2$, (d) 625, 2,000 h in sCO$_2$, (e) 740, 1,000 h in 17 bar steam and (f) 740, 4,000 h in 17 bar steam. (a-c) are etched in aqua regia.

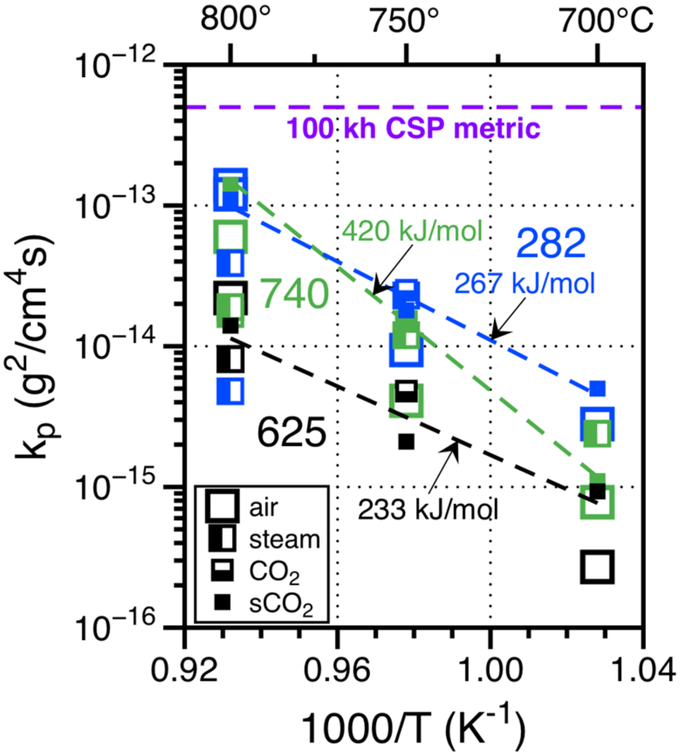

Figure 4. Arrhenius plot of parabolic rate constants measured in this study in four environments.

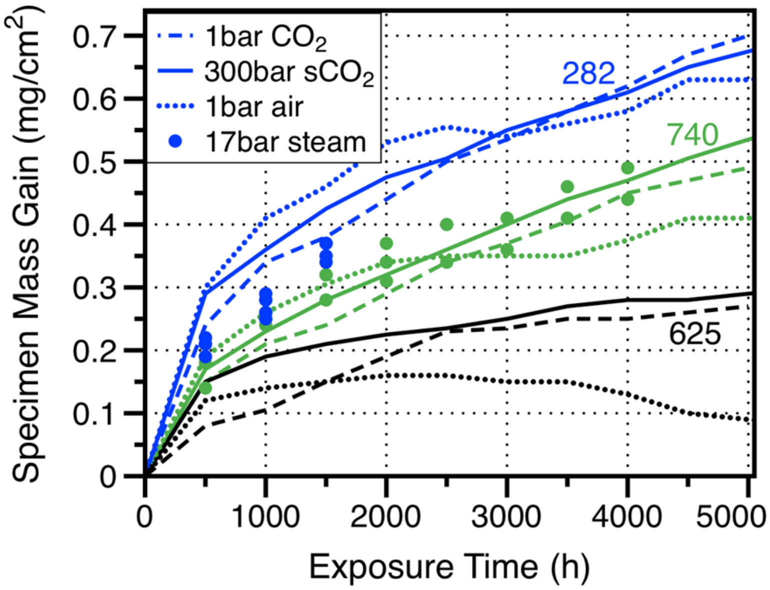

Figure 5. Specimen mass change data at 750°C for alloy specimens in four environments.

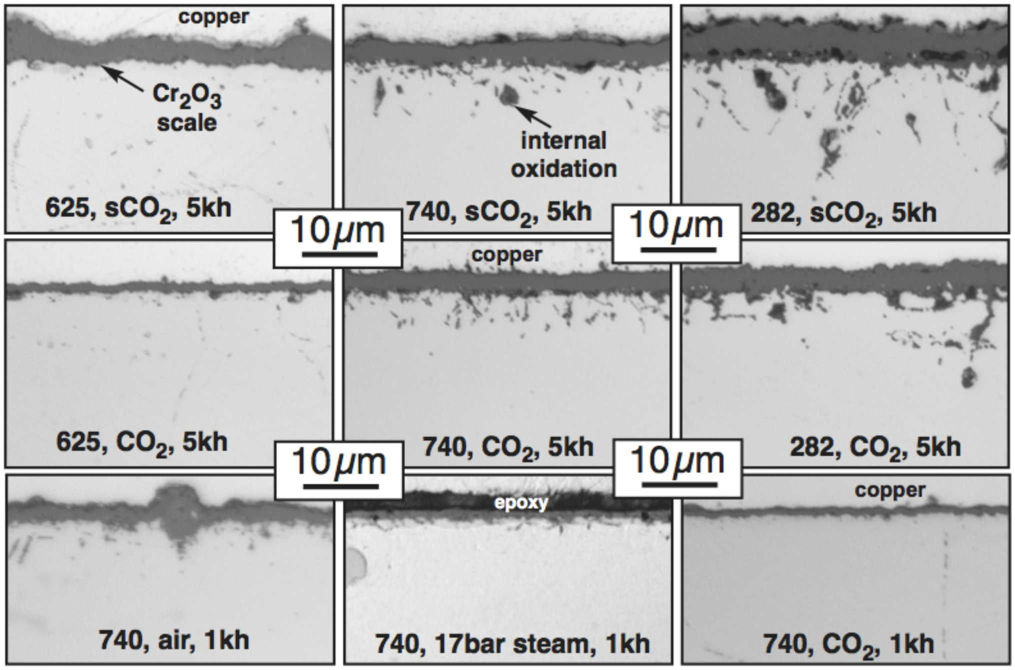

Figure 6. Light microscopy of specimens exposed at 750°C (a) 625, 5,000 h in sCO_2, (b) 740, 5,000 h in sCO_2, (c) 282, 5,000 h in sCO_2, (d) 625, 5,000 h in CO_2, (e) 740, 5,000 h in CO_2, (f) 282, 5,000 h in CO_2, (g) 740, 1,000 h in lab. Air, (h) 740, 1,000 h in 17 bar steam and (i) 740, 1,000 h in CO_2.

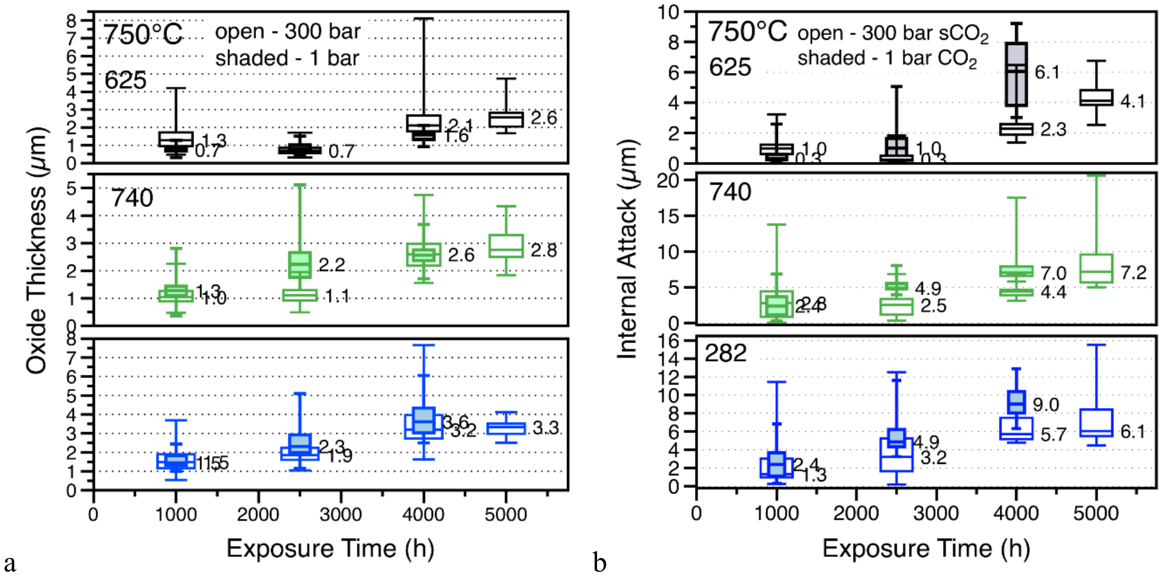

Figure 7. Box and whisker plots of the (a) oxide thickness and (b) depth of internal oxidation after exposures in 1 and 300 bar CO_2 at 750°C. The median value is shown.

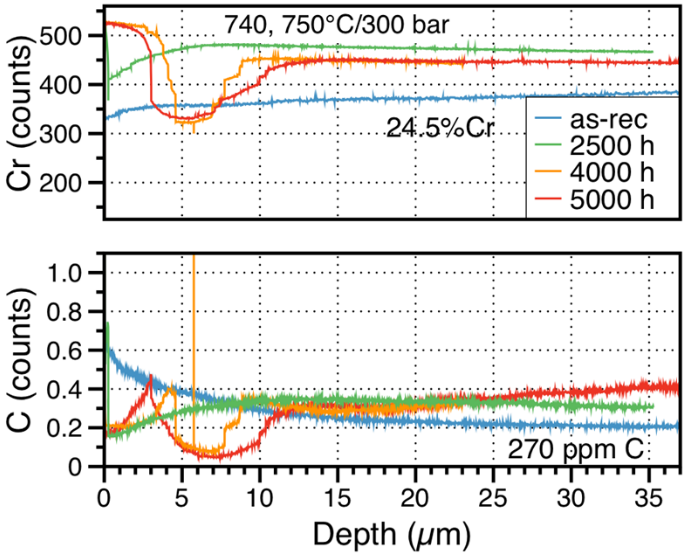

Figure 8. Glow discharge optical emission profiles for alloy 740 specimens exposed at 750°C to 300 bar sCO_2 for various times compared to an as-received specimen. There was no evidence of C ingress into the substrate after exposure but Cr depletion beneath the scale was evident.

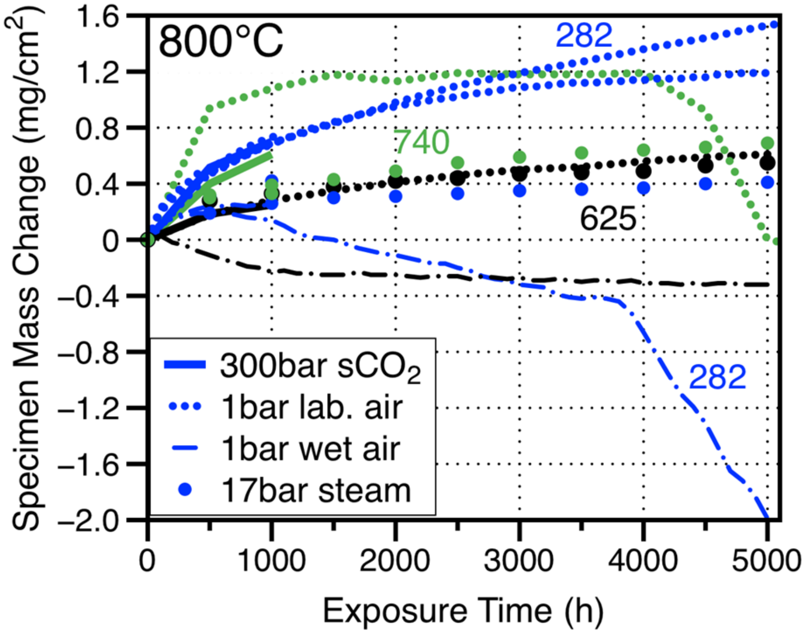

Figure 9. Specimen mass change data at 800°C for alloy specimens in four environments.

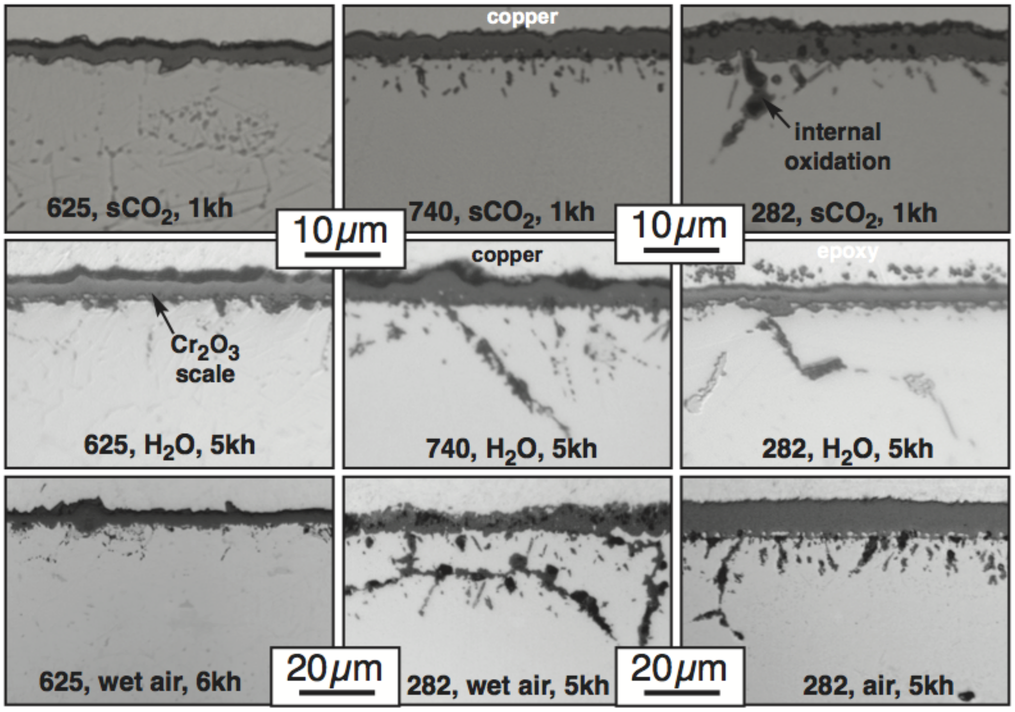

Figure 10. Light microscopy of specimens exposed at 800°C (a) 625, 1,000 h in sCO$_2$, (b) 740, 1,000 h in sCO$_2$, (c) 282, 1,000 h in sCO$_2$, (d) 625, 5,000 h in 17 bar steam, (e) 740, 5,000 h in 17 bar steam, (f) 282, 5,000 h in 17 bar steam, (g) 625, 6,000 h in wet air, (h) 282, 5,000 h in wet air and (i) 282, 5,000 h in lab. air.

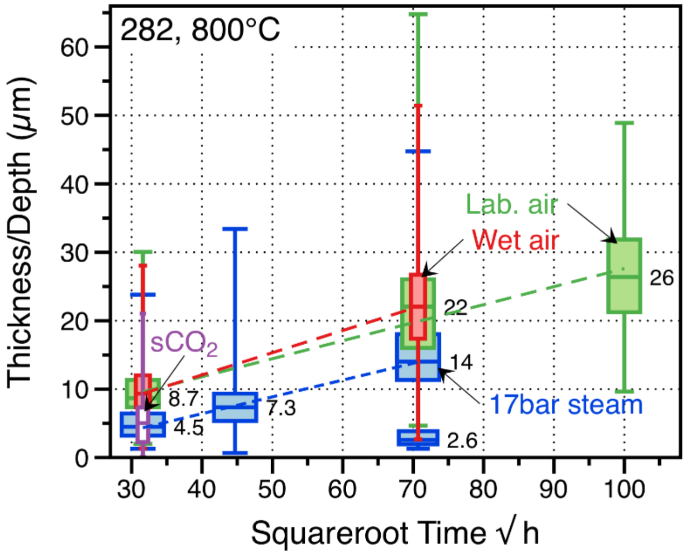

Figure 11. Box and whisker plots of the depth of internal oxidation on alloy 282 specimens after exposures in four environments. The median value is shown.

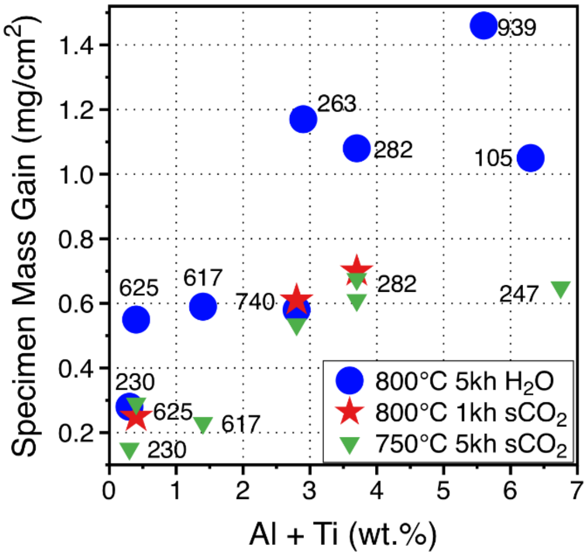

Figure 12. Specimen mass gain after several different exposures plotted versus the Al+Ti content of the alloys. All conditions show the same increasing trend.

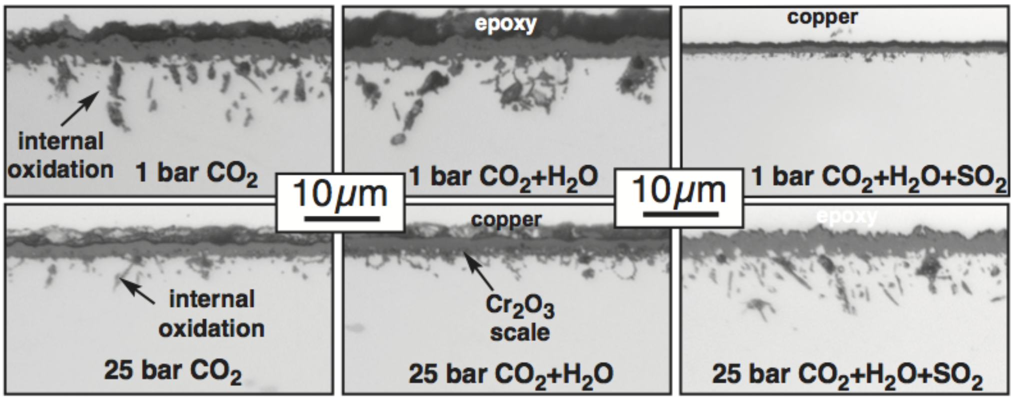

Figure 13. Light microscopy of alloy 282 specimens exposed for 500 h at 800°C at (a-c) 1 bar and (d-f) 25 bar in (a,d) high purity CO_2, (b,e) CO_2+10%H_2O and (c,f) CO_2+10%H_2O+0.1%SO_2.

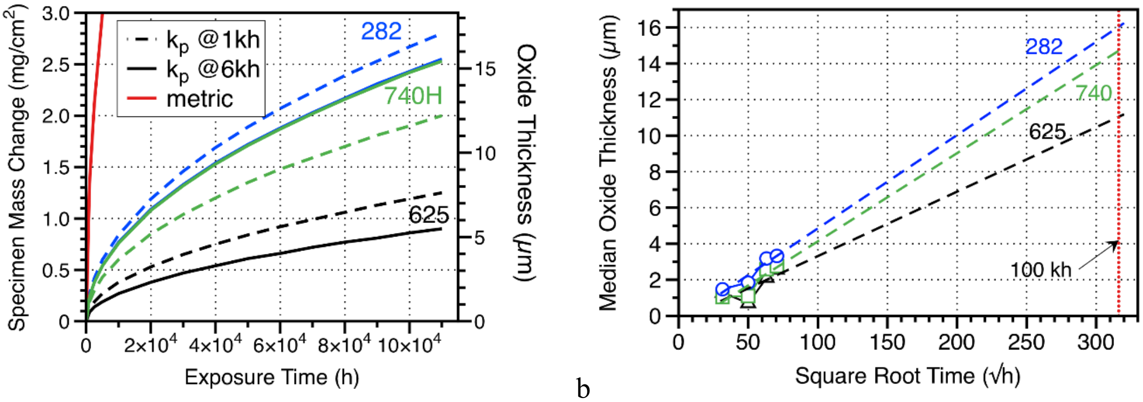

a

b

Figure 14. (a) Extrapolation of the rate constants determined at 750°C after 1,000 and 6,000 h exposures in 300 bar sCO_2. The mass gain can be converted to an oxide thickness assuming a dense Cr_2O_3 reaction product. (b) Extrapolation of the oxide thickness data observed at 1,000-5,000 h in 300 bar sCO_2 to 100,000 h assuming parabolic behavior. The oxide thickness values in (a) and (b) are similar and represent very thin oxides after extended service in this environment.